



Energy & Geoscience Institute

AT THE UNIVERSITY OF UTAH



COMPLETED IMMEDIATE DELIVERY

Principal Investigators:

Michal Nemčok, Ph.D.

Research Professor

Email: mnemcok@egi.utah.edu

Phone: +421-2-2062 0781

Samuel Rybár, Ph.D.

Co-Principal Investigator

Email: srybar@egi.utah.edu

Sponsors Receive

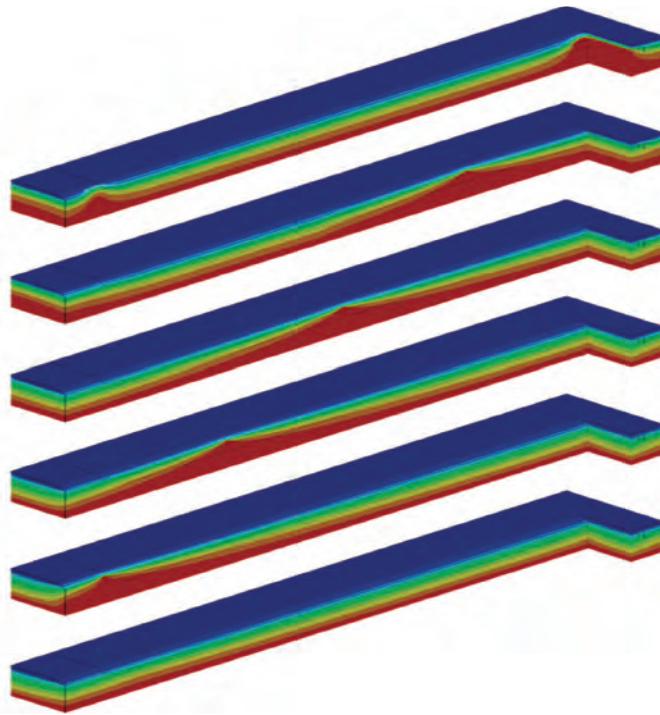
- *Analytics-ready Data*
- *ArcGIS Delivery*
- *Technical Workshop*
- *Full Report*

Sponsor Investment

\$65k (USD)

Project I 01341

Thermal History of Transform Margins



Dr. Michal Nemčok, Dr. Andreas Henk, Dr. Samuel Rybár, Dr. Lucia Ledvényiová,
Dr. Júlia Kotulová, Mgr. Dominika Godová, Mgr. Jana Rigová, Dr. Tamás Csibri,
Mgr. Matej Molčan, Dr. Štefánia Pramuková, , Mgr. Stanislaw Stanciaszek,
Mgr. Adam Baranowski, Bc. Tadeusz Gontar

EGI Energy & Geoscience Institute

I 01341



EMAIL:

ContactEGI@egi.utah.edu

PHONE: (801) 585-3826

EXECUTIVE SUMMARY

The main motivation for this study was to understand the thermal history of transform margins and spatial and temporal distribution of regions with a ductile lower crust. We completed another generation of thermal modeling, focused on how the thermal evolution of transform margins is controlled by deformation as ridge migration parallel to the margin causes a pronounced thermal perturbation. With respect to the structural architecture of transforms, described in detail in Chapters 1–3, one needs to understand that thermal history of transform margin *sensu stricto* is fundamentally different from that of both the associated and joining horse-tail structures. While the movements characterizing the transform *sensu stricto* are primarily parallel to the plate boundary, the movements characterizing the horse-tail structures in their normal fault-controlled portions are orthogonal to the ocean-continent boundary.

SPONSORS



Table of Contents

Chapter 1 Coromandal Transform Fault Zone	1
Introduction.....	2
Fault model of the continental side of the transform fault zone.....	4
Crustal model of the continental side of the transform fault zone.....	13
Fault model of the oceanic side of the transform fault zone	21
Crustal model of the oceanic side of the transform fault zone	23
Tectonic development and plate reconstruction.....	25
References	35
Chapter 2 Romanche Transform Fault Zone	37
Introduction.....	38
Fault model of the continental side of transform	40
Crustal model of the continental side of the transform fault zone.....	52
Fault model of the oceanic side of the transform fault zone	71
Crustal model of the oceanic side of the transform fault zone	77
Tectonic development and plate reconstruction.....	80
References	89
Chapter 3 Zenith-Wallaby-Perth Transform Fault Zone	95
Introduction.....	96
Fault model of the continental side of the transform fault zone.....	101
Crustal model of the continental side of transform	118
Fault model of the oceanic side of the transform fault zone	141
Crustal model of the oceanic side of transform.....	148
Plate reconstructions.....	150
References	155
Chapter 4 Models of Source Rock Distribution	159
Introduction.....	160
Source rocks in transform margin settings.....	162
Transform margin sensu stricto	168
Local transform margin segment inside the transform fault zone sensu stricto	178
Local pull-apart segment inside the transform fault zone sensu stricto	182
Associated horse-tail structure	189
Joining horse-tail structure	195
Source rock depositional model for the African Romanche transform fault zone.....	210
References	218

Chapter 5 Models of Reservoir Rock Distribution	223
Introduction.....	224
Sedimentological background	224
Interpretation of the reflection seismic image	225
Seismic facies analysis.....	229
Discussion	231
Conclusions and recommendations	236
References	237
Chapter 6 Thermal Regime of Transform Margins Developing from Oceanic-Continental Transforms.....	239
Introduction.....	240
Model setup.....	243
Thermal regime	248
Ductility history of lower crust.....	256
References	258
Appendix 1 Results of Thermal History Modeling#.....	263
2D Correlation diagrams of modeled scenarios	264
104 Ma snapshot.....	264
96 Ma snapshot	268
88 Ma snapshot	272
80 Ma snapshot	276
72 Ma snapshot	279
64 Ma snapshot	282
60 Ma snapshot	285
40 Ma snapshot	288
20 Ma snapshot	291
0 Ma snapshot	293
Passports of Modeled Scenarios	295
Notes – Passports of Modeled Scenarios	295
Ultra-slow spreading rate	295
Slow spreading rate.....	295
Intermediately fast spreading rate.....	296
Fast spreading rate	297
Ultra-slow spreading scenarios	298
Slow spreading scenarios	304

Intermediately fast spreading scenarios	310
Fast spreading scenarios	316
Appendix 2 EGI-Series Samples: Apatite UFT and (U-Th-Sm)/He Thermochronology	321
Report	321
1. Executive summary	22
2. Apatite Fission Track Age Data	345
3. Apatite Fission Track Length Data	355
Appendix A	380
Appendix B	390
Sampling strategy.....	397
Tectonic setting	401

List of Figures

Figure 1.1. a) Coromandal Transform geometry versus geometry of the pre-existing anisotropy (red rectangle), compared to those of the Romanche Transform (central panel) and Zenith-Wallaby-Perth Transform (right panel).....	2
Figure 1.1. b) Geological map (modified from Ray, 1963; Geological Survey of India, 1993) showing that the pre-existing weakness is represented by the Proterozoic orogenic belt.	3
Figure 1.2. a) Fault map of the Coromandal Transform margin with location of reflection seismic profiles, interpreted magnetic stripe anomalies, and offshore bathymetry and onshore topographic maps (modified from Nemčok et al., 2012a; Talwani et al., 2016).....	4
Figure 1.2. b) Study area with interpreted seismic profiles located on top of the Isostatic residual gravity anomaly map. Isostatic residual gravity anomaly map comes from Fugro (2006).....	5
Figure 1.2. c) Types of horse-tail structures of the Coromandal Transform zone connecting Cauvery and Krishna-Godavari rift zones.....	7
Figure 1.3. a) Reflection seismic profile CYD6-03-11 through the southern portion of the Coromandal transform fault zone sensu stricto.	8
Figure 1.3. b) NW-SE trending dip-oriented profile I-88-NEW054 through one of the failed pull-apart basins of the northern, associated, horse-tail structure.	9
Figure 1.3. c) WNW-ESE trending dip-oriented profile PRD03-21 through the northern, associated, horse-tail structure not too far from the Krishna-Godavari rifted margin.	10
Figure 1.3. d) Reflection seismic profile CYD6-10 showing a flower structure associated with a distinctively listric dextral Coromandal strike-slip fault dissecting the Cauvery Rift Zone inside the southern, joining, horse-tail structure.....	11
Figure 1.3. e) Reflection seismic profile GXT 800 PSTM showing structural highs at the junction of the Cauvery Rift Zone and Coromandal strike-slip fault zone, meeting each other in the joining horse-tail structure. This is the place where one can see structural highs with syn-rift fill on top of them, making them exceptionally good exploration prospects.....	12
Figure 1.4. a) Interpreted reflection seismic profile through the western portion of the failed Cauvery rift zone, which underwent only the stretching phase. Syn-rift sediment thickness maxima near their controlling faults, which are rather steeply dipping, reach 2–2.5 s TWT.	12

Figure 1.4. b) Interpreted reflection seismic profile through the eastern portion of the failed Cauvery rift zone, which underwent both stretching and thinning phases. Syn-rift sediment thickness maxima near their controlling faults, which have rather low dips, reach 0.5–1.5 s TWT.	13
Figure 1.5. a) Depth-to-the-basement top surface map of the Coromandal transform fault zone region.	14
Figure 1.5. b) Depth-to-the-basement top surface and fault maps of the Coromandal transform fault zone region.....	16
Figure 1.5. c) Highs and lows of the Coromandal transform zone, including its northern and southern horse-tail structures, highlighted in blue and red/dark blue, respectively, together with faults.	17
Figure 1.5. d) Highs of the northern horse-tail structure of the Coromandal transform zone highlighted by blue polygons together with faults. Note prominent NE-plunging noses of structural highs, which are rather broad. They characterize the associated horse-tail structure.....	18
Figure 1.5. e) Highs of the southern horse-tail structure of the Coromandal transform zone highlighted by blue polygons.	19
Figure 1.6. Thickness map of the continental crust of the Coromandal transform margin with location of the boundary between continental and oceanic crusts, on top of and offshore bathymetry and onshore topographic maps.	21
Figure 1.7. Fault map of the Coromandal transform margin with location of reflection seismic profiles, interpreted magnetic stripe anomalies, and offshore isostatic residual gravity anomaly and onshore topographic maps.....	22
Figure 1.8. a) Tectonic map of East India including boundaries between continental, proto-oceanic and oceanic types of crust (Sinha et al., 2016).	23
Figure 1.8. b). Reflection seismic profile through the southern portion of the northern, associated, horse-tail structure of the Coromandal transform fault zone, imaging three different types of crust, continental, proto-oceanic and oceanic (Nemčok et al., 2012b).	24
Figure 1.9. a) India-Elan Bank reconstruction (Sinha et al., 2016).	26
Figure 1.9. b) India-Elan Bank reconstruction along married interpreted reflection seismic profile pairs from conjugated margins (Sinha et al., 2016). The profile reconstruction is made for the Aptian time period (ca 123 Ma). Breaking-up extensional system has India in its hanging wall and Elan Bank in its footwall.	27
Figure 1.10. India-Antarctica-Australia plate reconstructions using software GPlates and rotation poles from Seton et al. (2012).	28
Figure 1.10. b) Jurassic-Cretaceous boundary (145 Ma).	28
Figure 1.10. c) latest Berriasian (140 Ma).....	29
Figure 1.10. d) Valanginian (135 Ma).	29
Figure 1.10. e) latest Hauterivian (130 Ma).....	30
Figure 1.10. f) Barremian-Aptian boundary (125 Ma).	31
Figure 1.10. g) Aptian (120 Ma).	32
Figure 1.11. Sketch showing the development of the Elan Bank microcontinent in NW-SE trending transect. (Sinha et al., 2016).	33
Figure 1.12. Step-wise India-Elan Bank-Antarctica reconstruction (Sinha et al., 2016).....	34

Figure 2.1. a) Romanche transform geometry versus geometry of the pre-existing anisotropy (red rectangle), compared to those of the Coromandal Transform (left panel) and Zenith-Wallaby-Perth Transform (right panel). 38

Figure 2.1. b) Geological map (Commission for the Geological Map of the World, UNESCO-ASGU, 1990) showing that the pre-existing weakness is represented by the Proterozoic pan-African orogenic belt. 39

Figure 2.2. a) Fault trace representation of faults shown in Figure 2.1b. Fault dips are indicated by teeth. 40

Figure 2.2. b) Types of horse-tail structures of the Romanche transform zone connecting it to two pull-apart terrains. 41

Figure 2.3. Location map of reflection seismic profiles constraining the fault pattern shown in Figure 2.2a. Left – our profiles, right – profiles from Antobreh et al. (2009)..... 42

Figure 2.4. a) Reflection seismic profile through the portion of the associated horse-tail structure of the Romanche transform zone in offshore Benin (Nemčok et al., 2012). 43

Figure 2.4. b) Interpreted reflection seismic section through the associated horse-tail structure in offshore Benin (Nemčok et al., 2004)..... 44

Figure 2.4. c) Interpreted reflection seismic image showing the transition of the associated horse-tail structure into the Romanche transform fault zone sensu stricto in offshore Benin (Nemčok et al., 2004).. 45

Figure 2.4. d) Interpreted reflection seismic profile G1B through the Romanche transform fault zone sensu stricto in Ghana (Nemčok et al., 2004)..... 45

Figure 2.4. e) Interpreted reflection seismic profile G1C through the Romanche transform fault zone sensu stricto in Ghana (Nemčok et al., 2004). 46

Figure 2.4. f) Interpreted reflection seismic profile G1D through the Romanche transform fault zone sensu stricto in offshore Ghana (modified from Nemčok et al., 2004). 47

Figure 2.4. g) Reflection seismic profile through one of the pull-apart basins located inside the joining horse-tail structure of the Romanche transform zone in offshore Ivory Coast (Nemčok et al., 2004)..... 48

Figure 2.4. h) Two interpreted reflection seismic profiles cutting through the joining horse-tail structure in the offshore Ivory Coast (Nemčok et al., 2004). 49

Figure 2.5. Map of the fault pattern and crustal architecture, offshore Togo and Benin (Nemčok et al., 2004).51

Figure 2.6. a) Location map of seismic and gravity transects through the Ghana Ridge (Sage et al., 2000). Thick line shows the transect from (b). 53

Figure 2.6.b) Combined seismic velocity distribution (normal numbers) based on refraction experiment and density distribution (numbers in italics) based on the forward gravity modeling along the transect through the Ghana Ridge (Sage et al., 2000). 54

Figure 2.7. a) Seismic transect location map. DOBS locations are shown by triangles (Edwards et al., 1997). Line 7 represents the transect shown in (b-d)..... 55

Figure 2.7. b) Seismic velocity distribution model based on refraction experiment along the transect through the Ghana Platform (Edwards et al., 1997). Velocities are in kms^{-1} 55

Figure 2.7. c) Density distribution model based on forward gravity modeling along the refraction experiment along the transect through the Ghana Platform (Edwards et al., 1997). 56

Figure 2.7. d) Magnetization distribution model based on forward magnetic modeling along the refraction experiment along the transect through the Ghana Platform (Edwards et al., 1997). Magnetizations are in A m^{-1} 57

Figure 2.8. a) Location map of gravity-modelled transects from (b-f) on top of Free-air gravity (upper panel) and Bouguer gravity anomaly maps (lower panel) (Antobreh et al., 2009). Free-air map shows a 1 x 1 min grid satellite-radar altimeter data. Bouguer map is a 400 km high-pass filtered version. .58

Figure 2.8. b-c) Gravity-modeled transects A and B through the Romanche transform margin (Antobreh et al., 2009). (See Figure 2.8a for profile locations). 59

Figure 2.8. d-e) Gravity-modeled transects C and D through the Romanche transform margin (Antobreh et al., 2009). (See Figure 2.8a for profile locations). 60

Figure 2.8. f) Gravity-modeled transect E through the Romanche transform margin (Antobreh et al., 2009).. (See Figure 2.8a for profile locations). 61

Figure 2.9. a) Location map of reflection seismic profiles through the Romanche transform margin in offshore Ghana interpreted by Antobreh et al. (2009) on top of regional tectonic map. 63

Figure 2.9. b-c) Geological cross sections 1 and 2 through the western horse-tail structure interpreted along reflection seismic profiles shown in (a) (Antobreh et al., 2009). 64

Figure 2.9. d-f) Geological cross sections 3, 4 and 5 through the Romanche transform fault zone sensu stricto interpreted along reflection seismic profiles shown in (a) (Antobreh et al., 2009). 65

Figure 2.9. g-h) Geological cross sections 6 and 7 through the Romanche transform fault zone sensu stricto interpreted along reflection seismic profiles shown in (a) (Antobreh et al., 2009). 66

Figure 2.9. i-k) Geological cross sections 8-10 through the eastern horse-tail structure interpreted along reflection seismic profiles shown in (a) (Antobreh et al., 2009). 67

Figure 2.10. a) Depth to the top of pre-rift map in s TWT with its controlling fault pattern (Staniaszek, 2020, unpublished student project based on data taken from (Nemčok et al., 2004, 2014; Antobreh et al., 2009). 68

Figure 2.10. b) Fault pattern interpreted from the reflection seismic grid in offshore Ghana on top of the contour map showing the depth in s TWT to the top of the syn-rift strata. (Antobreh et al., 2009). 69

Figure 2.10. c) Depth to the top of basement map (Baranowski, 2020, unpublished student project based on data taken from (Edwards et al., 1997; Sage et al., 2000; Nemčok et al., 2004, 2014; Antobreh et al., 2009). 69

Figure 2.10. d) Depth to Moho map (Baranowski, 2020, unpublished student project based on data taken from (Edwards et al., 1997; Sage et al., 2000; Antobreh et al., 2009). 70

Figure 2.10. e) Continental crustal thickness map (Baranowski, 2020, unpublished student project based on maps shown in Figures 2.10c-d). 70

Figure 2.11 a) Free-air gravity data on the oceanic crust of the Equatorial Atlantic (Commission for the Geological Map of the World, Africa, 1990, Commission for the Geological Map of the World, South America, 2000; Sandwell and Smith, 1997). 72

Figure 2.11 b) Shaded free-air gravity data on the oceanic crust of the Equatorial Atlantic (commission for the Geological Map of the World, Africa, 1990; Commission for the Geological Map of the World, South America, 2000; Sandwell and Smith, 1997). 72

Figure 2.11. c) Hill-shaded free-air gravity map of the oceanic crust of the Gulf of Guinea (data from Commission for the Geological Map of the World, Africa, 1990; Sandwell and Smith, 1997). 73

Figure 2.11. d) Free air/free air gravity combination map of the oceanic crust of the Gulf of Guinea (Commission for the Geological Map of the World, Africa, 1990; Sandwell and Smith, 1997; AOA Geophysics, 2000). 73

Figure 2.11. e) Enhanced free air/free air gravity combination map of the oceanic crust of the Gulf of Guinea (Commission for the Geological Map of the World, Africa, 1990; Sandwell and Smith, 1997; AOA Geophysics, 2000).....74

Figure 2.11. f) Bouguer/free air gravity combination map of the oceanic crust of the Gulf of Guinea (Commission for the Geological Map of the World, Africa, 1990; Sandwell and Smith, 1997; AOA Geophysics, 2000).....74

Figure 2.11. g) Bouguer gravity anomaly map of the oceanic crust of the Gulf of Guinea draped over the bathymetry map (gravity from AOA Geophysics, 2000).....75

Figure 2.11. h) Isostatic residual anomaly/free air gravity/crust age combination map of the oceanic crust of the Gulf of Guinea (Commission for the Geological Map of the World, Africa, 1990; Sandwell and Smith, 1997; AOA Geophysics, 2000).....75

Figure 2.11. i) Isostatic residual anomaly/free air gravity combination map of the oceanic crust of the Gulf of Guinea (Commission for the Geological Map of the World, Africa, 1990; Sandwell and Smith, 1997; AOA Geophysics, 2000).....76

Figure 2.11. j) Enhanced isostatic residual gravity anomaly map of the oceanic crust of the Gulf of Guinea (AOA Geophysics, 2000).....76

Figure 2.12. Map of the Equatorial Atlantic oceanic crust age based on magnetic anomaly data and plate reconstructions for magnetically quiet zones, combined with geology of adjacent continents (maps are from Commission for the Geological Map of the World, Africa, 1990, South America, 2000; Müller et al., 1997).77

Figure 2.13. Oceanic crustal thickness map (Baranowski, 2020, unpublished student project based on maps shown in Figures 2.10c-d).....80

Figure 2.14. Closing match of Brazilian and African oceanic/continental crustal boundaries restored for different times of the 105–110 (Albian) interval for different segments of the Equatorial Atlantic (Nemčok et al., 2004).82

Figure 2.15. a-b)Equatorial Atlantic plate reconstructions using software GPlates and rotation poles from Seton et al. (2012).83

Figure 2.15. c) mid-Albian (105 Ma).84

Figure 2.15. d) latest Albian (100 Ma).....84

Figure 2.15. e) Cenomanian (95 Ma).84

Figure 2.15. f) Turonian (90 Ma).84

Figure 2.15. g) Santonian (85 Ma).85

Figure 2.15. h) early Campanian (80 Ma).....85

Figure 2.15. i) late Campanian (75 Ma).85

Figure 2.16. The geodynamic position of Ghana Ridge with time (modified from Edwards et al., 1997).86

Figure 3.1. a) Zenith-Wallaby-Perth transform geometry versus geometry of the pre-existing anisotropy (red rectangle, right panel), compared to those of the Coromandal Transform (left panel) and Romanche Transform (central panel).96

Figure 3.1. b) Automatic gain control of the Isostatic residual (central panel) and total horizontal derivative of the Free air (right panel) gravity anomaly maps (modified from Nemčok et al., 2015) showing pre-existing weaknesses represented by the Permian rift branch and Jurassic continental strike-slip fault zone.97

Figure 3.2. a) Location map of the Zenith-Wallaby-Perth transform fault zone (Zeewyk-Houtman trend or red rectangle) with indication of key dredges and wells used for its study (Nemčok et al., 2015).98

Figure 3.2. b) Location of offshore basins in Western and Northwestern Australia (modified from <http://www.ga.gov.au/scientific-topics/energy/province-sedimentary-basin-geology/petroleum>). 99

Figure 3.2. c) Line determination of the ocean-continent boundary (ocb) determined synthetically from seismic, gravity and magnetic data posted on top of the Total magnetic intensity map corrected to pole, having 2 km resolution (Nemčok et al., 2015).100

Figure 3.2. d) Main faults of the Zenith-Wallaby-Perth transform fault zone and its neighboring rift margin segments, which reside in the continental crust, shown on top of topography and bathymetry maps (modified from Nemčok et al., 2020).101

Figure 3.2. d - continuation) Main faults of the Zenith-Wallaby-Perth transform fault zone and the neighboring rift margin segments, that reside in the continental crust, shown on top of topography and bathymetry maps (modified from Nemčok et al., 2020).102

Figure 3.2. e) Main faults of the Zenith-Wallaby-Perth transform fault zone and the neighboring rift margin segments, that reside in the oceanic crust, shown on top of digital elevation model (DEM taken from Nemčok et al., 2015).103

Figure 3.3. a) Location map of reflection seismic profiles constraining the fault pattern shown in Figure 3.2d on top of the total magnetic intensity map with 2 km resolution (modified from Nemčok et al., 2015). 104

Figure 3.3. b) Location map of reflection seismic profiles constraining the fault pattern shown in Figure 3.2d on top of the bathymetry map (modified from Nemčok et al., 2015).....105

Figure 3.3. c) Location map of wells constraining our interpretation of seismic profiles from Figures 3.3a-b on top of the bathymetry map (Nemčok et al., 2015).105

Figure 3.4. a) E-W striking profile hb01-106p through the Zenith-Wallaby-Perth transform fault zone sensu stricto.106

Figure 3.4. b) WNW-ESE striking profile 057rf-08 through the two major strike-slip fault zones (purple faults) representing the Zenith-Wallaby-Perth transform fault zone sensu stricto and their overlap region. 107

Figure 3.4. c) E-W striking profile s310-s310_35 through the two major strike-slip fault zones (purple faults) representing the Zenith-Wallaby-Perth transform fault zone sensu stricto and their overlap region further south of (b).108

Figure 3.5. a) E-W striking profile s310-32 through the Southeastern horse-tail structure of the Zenith-Wallaby-Perth transform fault zone (purple faults).109

Figure 3.5. b) E-W striking profile s310-31 through the Southeastern horse-tail structure further south from the profile in 3.5. a). See 3.5. a for further explanation.110

Figure 3.5. c) NW-SE striking profile s81r-81r-13 through the Southeastern horse-tail structure further south from profile in 3.5. b).111

Figure 3.6. a) Profile s310-50 cutting through the area where the Northwestern horse-tail structure starts to splay off from the Zenith-Wallaby-Perth transform fault zone.111

Figure 3.6. b) Profile through the Northwestern horse-tail structure of the Zenith-Wallaby-Perth transform fault zone. Profile 135-08 – detail.112

Figure 3.7. a) Interpreted Free-air gravity anomaly map from Nemčok et al. (2015). Values are in mGal. Sj and Sn – Sonja and Sonne ridges.114

Figure 3.7. b) Contour map of the Free-air gravity anomalies with 5 mGal contour interval (Nemčok et al., 2015).....114

Figure 3.7. c) Interpreted Total horizontal derivative map of the Free-air gravity anomalies from Nemčok et al. (2015). See 3.7.a for remaining captions.115

Figure 3.7. d) Interpreted 1st vertical derivative map of the Free-air gravity anomalies from Nemčok et al. (2015). See 3.7.a and 3.7.b for remaining captions.....116

Figure 3.7. e) Interpreted Dip azimuth map of the 1st derivative of the Free-air gravity anomalies from Nemčok et al. (2015). See 3.7.a and 3.7.b for remaining captions.117

Figure 3.7. f) Free-air offshore and Bouguer onshore gravity anomaly maps imported into Petrel project (Nemčok et al., 2015).118

Figure 3.7. g) Contour Bouguer anomaly map. with 2x2 km resolution (Nemčok et al., 2015). Contour interval is 1 mGal. Dark green and red colors are at positive and negative ends of the spectrum.....119

Figure 3.7. h) Interpreted Isostatic residual gravity anomaly map with 2x2 km resolution from Nemčok et al. (2015). See 3.7.a for captions.....120

Figure 3.7. i) Interpreted Total horizontal derivative map of the Isostatic residual gravity anomalies from Nemčok et al. (2015). See 3.7.a and 3.7.b for captions.122

Figure 3.7. j) Interpreted 1st vertical derivative of the Isostatic residual gravity anomaly map from Nemčok et al. (2015). See 3.7.a for captions.....123

Figure 3.7. k) Interpreted Automatic gain contribution to the Isostatic residual gravity anomalies from Nemčok et al. (2015). See 3.7.a for captions.124

Figure 3.8. Profile s135-s135_09 through the Zenith-Wallaby-Perth transform fault zone juxtaposing the Wallaby Plateau to oceanic crust; i.e., to the northwest of the Northwestern horse-tail structure. 125

Figure 3.9. a) Combined reflection seismic, gravity and magnetic profile through the Southeastern horse-tail structure of the Zenith-Wallaby-Perth transform fault zone (Nemčok et al., 2020).126

Figure 3.9. b) Combined reflection seismic, gravity and magnetic profile through the southeastern portion of the Zenith-Wallaby-Perth transform fault zone (Nemčok et al., 2020).127

Figure 3.9. c) Combined reflection seismic, gravity and magnetic profile through the southeastern portion of the Zenith-Wallaby-Perth transform fault zone (Nemčok et al., 2020).128

Figure 3.9. d) Combined NW-SE striking reflection seismic, gravity and magnetic profile through the Cuvier extensional margin, which was controlled by the extensional end of the initial Northwestern horse-tail structure of the Zenith-Wallaby-Perth transform fault zone, and the oceanic crust to the NE of the Wallaby Plateau (Nemčok et al., 2020). Isostatically compensated magmatic ridges in the NW represent the Sonja and Sonne ridges.129

Figure 3.9. e) Combined reflection seismic, gravity and magnetic profile through the portion of the Zenith-Wallaby-Perth transform fault zone, which is further oceanward from its initial Northwestern horse-tail structure (Nemčok et al., 2020).130

Figure 3.10. a) Georeferenced raster and digitized maps from Müller et al. (2005) in the ArcGIS for this project. 131

Figure 3.10. b continued) Georeferenced raster and digitized maps from Müller et al. (2005) in the ArcGIS for this project.132

Figure 3.10. c) Georeferenced raster and digitized maps from Salmon et al. (2013) in the ArcGIS project.133

Figure 3.10. d) Cross-checked databases of Salmon et al. (2013) with those of Reading and Kennett (2003), Reading et al. (2003, 2012) and Müller et al. (2005), using locations of their data points.....134

Figure 3.10. e) Comparison of our crustal thickness map with that of Salmon et al. (2013). Location of constraining data points is shown by black dots. Blue and red show the maximum and minimum crustal thickness, respectively.....134

Figure 3.10. f) Point determination of the ocean-continent boundary from individual reflection seismic profiles posted on the Isostatic residual gravity anomaly map, having 2 km resolution (Nemčok et al., 2015).....135

Figure 3.10. g) Probability zone determination of the ocean-continent boundary determined synthetically from seismic, gravity and magnetic data posted on top of the Free-air gravity map, having 2 km resolution (Nemčok et al., 2015).136

Figure 3.10. h) Match of the crustal thickness contour map with ocean-continent boundary map (Nemčok et al., 2015).137

Figure 3.10. i) Contoured crustal thickness map together with ocean-continent boundary map and Isostatic residual gravity anomaly map from (3.10f) (Nemčok et al., 2015).138

Figure 3.10. j) Interpreted reflection seismic profile through the Exmouth Plateau, which is characterized by a stretching zone (blue accommodating faults) in its proximal portion and thinning zone (green accommodating faults) in its distal portion.139

Figure 3.10. k) Map of the areal extent of the thinning zone (light yellow polygon) determined from interpreted reflection seismic profiles, showing isostatic residual gravity anomalies from (3.10f), crustal thickness, ocean-continent boundary and a stick map showing the extent of the thinning zone in individual seismic profiles through the initial transform margin.....140

Figure 3.11. a) Oceanic crust age contour map (Müller et al., 2008).....142

Figure 3.11. b) The interpreted correction to pole map of the Total magnetic intensity with 2 x 2 km resolution from Nemčok et al. (2015) showing the main ridge- and trough-controlling faults in black.142

Figure 3.11. c) Transparent correction to pole map of the total magnetic intensity with 2 x 2 km resolution together with location of exploration reflection seismic grids (Nemčok et al., 2015).....144

Figure 3.11. d) Total horizontal derivative of the total magnetic intensity map (Nemčok et al., 2015).....145

Figure 3.11. e) Interpreted 1st vertical derivative map of the total magnetic intensity from Nemčok et al. (2015). 147

Figure 3.12. a) NW-SE striking profile s310-72 through the two overstepping transform fault zones (purple) of the Zenith-Wallaby-Perth transform fault zone.148

Figure 3.12. b) WNW-ESE profile 57r-04 through the overstepping strike-slip fault zones (purple faults) of the Zenith-Wallaby-Perth transform fault zone and the successful pull-apart basin in the overstep, making it to the break-up. Adjacent oceanic crust (orange top) contains distinct ridges and troughs separated by uninterpreted steeply-dipping faults. The elevation difference reaches up to 2 s TWT.149

Figure 3.13. a) India-Antarctica-Australia plate reconstructions using software GPlates and rotation poles from Seton et al. (2012).151

Figure 3.13. b) Jurassic-Cretaceous boundary (145 Ma).153

Figure 3.13. c) latest Berriasian (140 Ma).153

Figure 3.13. d) Valanginian (135 Ma).154

Figure 3.13. e) latest Hauterivian (130 Ma).154

Figure 3.13. f) Barremian-Aptian boundary (125 Ma).155

Figure 3.13. g) Aptian (120 Ma).155

Figure 4.1. a) Depth-to-the-basement top surface and fault maps of the Coromandal transform fault zone region.....163

Figure 4.1. b) Depth-to-top basement map of the Coromandal transform fault zone with indication of sediment transport pathways (red) and sediment-trapping basins (yellow).164

Figure 4.2. a) Highs of the northern horse-tail structure of the Coromandal transform zone highlighted by blue polygons together with faults.165

Figure 4.2. b) Depth-to-top basement map of the associated horse-tail structure of the Coromandal transform fault zone with indication of sediment transport pathways and sediment-trapping basins.165

Figure 4.3. a) Highs of the southern horse-tail structure of the Coromandal transform zone highlighted by blue polygons.166

Figure 4.3. b) Depth-to-top basement map of the joining horse-tail structure of the Coromandal transform fault zone indicating sediment transport pathways and sediment-trapping basins.....166

Figure 4.4. a) Faults of the African Romanche transform margin with boundary between oceanic and continental crusts (Staniaszek, 2019, unpublished student project based on data taken from (Nemčok et al., 2004, 2014, Antobreh et al., 2009).167

Figure 4.4. b) Depth-to-basement map of the African Romanche transform margin (Nemčok et al., 2004). Note the Pan-African orogenic belt front indicated by thrust faults outcropping in onshore Ghana.167

Figure 4.4. c) Depth-to-pre-rift map of the African Romanche transform margin with main controlling fault pattern (Staniaszek, 2019, unpublished student project based on data taken from (Nemčok et al., 2004, 2014, Antobreh et al., 2009).169

Figure 4.4. d) Depth-to-pre-rift map of the African Romanche transform margin with main controlling fault pattern from Figure 4.4c with indicated sediment transport pathways (red).169

Figure 4.5. a) Depth-to-pre-rift map of the associated horse-tail structure of the African Romanche transform margin with structural highs highlighted by light blue polygons. Red dotted line – OCB.....170

Figure 4.5. b) Depth-to-pre-rift map of the associated horse-tail structure of the African Romanche transform margin with indicated sediment transport (solid red).170

Figure 4.6. a) Fault map of the joining horse-tail structure of the African Romanche transform margin with structural highs highlighted by light blue polygons. Red dotted line – OCB.171

Figure 4.6. b) Depth-to-pre-rift map of the joining horse-tail structure of the African Romanche transform margin with indicated sediment transport (solid red), and sediment traps (red polygons).172

Figure 4.7. a) Interpreted reflection seismic profile G1B through the Romanche transform fault zone sensu stricto in Ghana (Nemčok et al., 2004).....172

Figure 4.7. b) Contour map of the continental crust thickness of the African Romanche transform margin (Staniaszek, 2019, unpublished BS student project based on data taken from Commission for the Geological Map of the World, 1990; Edwards et al., 1997; Sage et al., 2000; Nemčok et al., 2004; Antobreh et al., 2009).173

Figure 4.7. c) Thickness map of the continental crust of the Coromandal transform margin constrained by a grid of ultra-deep reflection seismic images from IndiaSpan East, Phase 1 program (ION/GX

Technology, 2007), with location of cc/oc boundary, on top of and offshore bathymetry and onshore topographic maps.....174

Figure 4.8. a) Plate reconstruction of the Equatorial Atlantic made for late Albian (104 Ma, Antobreh et al., 2009) compared with thickness contour map of the Lower Cretaceous strata in the progressively opening oceanic basin located between oceanic-continental St Paul and Romanche transform fault zones prior to the final separation of the two drifting-apart continents (Nemčok et al., 2014). 175

Figure 4.8. b) Plate reconstruction of the Equatorial Atlantic made for Albian-Cenomanian boundary (100 Ma) compared with a thickness contour map of the middle Cretaceous strata in the progressively opening oceanic basin located between oceanic-continental St Paul and Romanche transform fault zones during the final separation of the two drifting-apart continents (Nemčok et al., 2014). 175

Figure 4.8. c) Plate reconstruction of the Equatorial Atlantic made for middle Cenomanian (96 Ma) (Nemčok et al., 2014).176

Figure 4.8. d) Plate reconstruction of the Equatorial Atlantic made for late Turonian (92 Ma) (Nemčok et al., 2014).176

Figure 4.8. e) Plate reconstruction of the Equatorial Atlantic made for late Campanian (76 Ma) (Nemčok et al., 2014).177

Figure 4.9. a) NW-SE trending dip-oriented profile through one of the pull-apart basins between two strike-slip faults in the northern portion of the Coromandal Transform (Nemčok et al., 2008).177

Figure 4.9. b) E-W striking profile s310-s310_35 through the two major strike-slip fault zones (purple faults) representing the Zenith-Wallaby-Perth transform fault zone sensu stricto and their overlap region further south of (b) (Nemčok et al., 2015b).179

Figure 4.10. a) Contour map of the depth to basement for the African Romanche transform margin indicating the location and timing of the laterally passing spreading center.....180

Figure 4.10. b) Contour map of the depth to Moho for the African Romanche transform margin indicating the location and timing of the laterally passing spreading center together with geological map (Commission for the Geological Map of the World, 1990)......180

Figure 4.10. c) Contour map of the continental and oceanic crust thickness for the African Romanche transform margin.....181

Figure 4.11. C_{Org} data from well 1_MAS_006 (Nemčok et al., 2012d).181

Figure 4.12. a) C_{Org} data from well 1_MAS_001 (Nemčok et al., 2012d).....183

Figure 4.12. b) S₁ data from well 1_MAS_001 (Nemčok et al., 2012d).183

Figure 4.12. c) S₂ data from well 1_MAS_001 (Nemčok et al., 2012d).....184

Figure 4.12. d) HI versus Tmax data from well 1_MAS_001 (Nemčok et al., 2012d).184

Figure 4.13. a) C_{Org} data from well 1_MAS_004 (Nemčok et al., 2012d).....185

Figure 4.13. b) S₁ data from well 1_MAS_004 (Nemčok et al., 2012d).185

Figure 4.13. c) S₂ data from well 1_MAS_004 (Nemčok et al., 2012d).....186

Figure 4.13. d) HI versus Tmax data from well 1_MAS_004 (Nemčok et al., 2012d).186

Figure 4.14. a) TOC data from cutting from well NAK-1 (from data donated by Ophir, 19th April 2015).188

Figure 4.14. b) TOC data from sidewall cores from well NAK-1 (from data donated by Ophir, 19th April 2015).189

Figure 4.15. a) Paleoenvironmental model for Albian-early Cenomanian time period (Kanungo et al., 2012).191

Figure 4.15. b) Paleoenvironmental model for middle Campanian time period (Kanungo et al., 2012).....192

Figure 4.15. c) Paleoenvironmental model for early Maastrichtian time period (Kanungo et al., 2012).193

Figure 4.16. a1) TOC data from ODP Leg 159 Site 959 (data taken from Kanungo et al., 2012).....198

Figure 4.16. a2) TOC data from ODP Leg 159 Site 959 (data taken from Kanungo et al., 2012) – detail along the horizontal axis.....199

Figure 4.16. b) S₁ data from ODP Leg 159 Site 959 (data taken from Kanungo et al., 2012).....200

Figure 4.16. c1) S₂ data from ODP Leg 159 Site 959 (data taken from Kanungo et al., 2012).201

Figure 4.16. c2) S₂ data from ODP Leg 159 Site 959 (data taken from Kanungo et al., 2012) – detail along the horizontal axis.....202

Figure 4.16. d) HI versus Tmax data from ODP Leg 159 Site 959 (data taken from Kanungo et al., 2012).203

Figure 4.17. a1) TOC data from ODP Leg 159 Site 960 (data taken from Kanungo et al., 2012).....204

Figure 4.17. a2) TOC data from ODP Leg 159 Site 960 (data taken from Kanungo et al., 2012) – detail along the horizontal axis.....205

Figure 4.17. b) S₁ data from ODP Leg 159 Site 960 (data taken from Kanungo et al., 2012).....206

Figure 4.17. c) S₂ data from ODP Leg 159 Site 960 (data taken from Kanungo et al., 2012).....207

Figure 4.18. a) TOC data from ODP Leg 159 Site 962 (data taken from Kanungo et al., 2012).208

Figure 4.18. b) S₁ data from ODP Leg 159 Site 962 (data taken from Kanungo et al., 2012).....209

Figure 4.18. c) S₂ data from ODP Leg 159 Site 962 (data taken from Kanungo et al., 2012).....210

Figure 4.18. d) HI versus Tmax data from ODP Leg 159 Site 962 (data taken from Kanungo et al., 2012).212

Figure 4.19. Location map of ODP Leg 207 (yellow box) with seismic and lithologic information from Well A2-1 (B), C/N versus TOC values for well 1257 (C), and HI versus Tmax values for Site 1257 (D) (Nemčok et al., 2013).215

Figure 5.1. Left panel: Location map of IndiaSpan reflection seismic profiles and arbitrary profiles extracted from several East Indian 3D seismic volumes (modified from Nemčok et al., 2007, 2008, 2012; ION/GX Technology, 2007; Sinha, 2014; Sinha et al., 2016). The world imagery on the background comes from Esri, DigitalGlobe, GeoEye, Earthstar Geographics, CNES/Airbus DS USDA, USGE, AeroGRID nad IGN. Right Panel: Lithostratigraphic and petroleum systems chart (Yanqun et al., 2017).....224

Figure 5.2. Idealized profile through the continental shelf and slope during the period of maximum separation between individual clinoform types (modified from Pellegrini et al., 2020).226

Figure 5.3. Scale-independent growth dynamics in clinoforms and their idealized grain-size classification (modified from Patruno and Helland-Hansen, 2018).226

Figure 5.4. Termination of reflections at lower and upper boundaries (Mitchum et al., 1977).227

Figure 5.5. Within-sequence reflection configurations (modified after Mitchum et al., 1977).....228

Figure 5.6. Reflection attributes (modified after Badley, 1985).229

Figure 5.7. External-form groups of sequences and seismic facies units (modified from Mitchum et al., 1977). 229

Figure 5.8. The key seismic facies identified in the reflection seismic image.232

Figure 5.9. Areal distribution of key seismic facies identified in the reflection seismic imagery.	233
Figure 5.10. Interpreted areal distribution of deltas, alluvial fans, fan deltas and mass transport deposits in the Cauvery Basin correlated with areas with pronounced syn-rift strata thickness provided the syn-rift strata isopach map. See Figures 5.8, 5.9 for more explanations.	234
Figure 5.11. Interpretation of areal distribution of deltas, alluvial fans, fan deltas and mass transport deposits in the Coromandal Transfer Fault Zone and Krishna-Godavari Basin region correlated with areas with pronounced syn-rift strata thickness provided by the syn-rift strata isopach map.....	235
Figure 6.1. Comparison between the evolution of a rifted and a transform margin.	242
Figure 6.2. A 3D finite element model used to study the thermal evolution of transform margins.	245
Figure 6.3. (next page to the right) Lithospheric temperature field in the fixed part of the 3D model for selected moments in time.	248
Figure 6.4. Surface heat flow in the fixed part of the 3D model for selected moments in time.	251
Figure 6.5. Surface heat flow evolution with time for points along three transects perpendicular to the transform margin (see inset for location).	253
Figure 6.6. Surface heat flow with time shown for six points located along a transform-parallel transect located 5.2 km landwards from the transform fault (see inset for location).	254
Figure 6.7. Parts of the lower continental crust with effective viscosities of less than 10^{18} Pa s shown by iso-surfaces for selected moments in time.	257

List of Tables

Table 2.1. a) Sea-floor spreading rate categories (e.g., Small, 1998; Dick et al., 2003; Kriner et al., 2006).....	39
Table 2.1. b) Implied transform fault slip categories.....	39
Table 2.2. a) Changes of the divergence during the activity of oceanic fractures zones (Nemčok et al., 2012).	87
Table 2.2. b) Timing of the change of divergence trajectories from NE-SW to E-W indicated by the geometry of the oceanic fracture zones.	88
Table 4.1. a) Criteria for ranking source rock and richness (Eggbowawaye, 2017).....	161
Table 4.1. b) Hydrocarbon generation and maturity measurement using vitrinite reflectance (Eggbowawaye, 2017).....	161
Figure 4.1. c) Interpretation of Hydrogen Index (HI) and Oxygen Index (OI) values to determine Kerogen types (Eggbowawaye, 2017).	161
Table 4.1. d) Geochemical parameters describing the level of thermal maturation (Eggbowawaye, 2017).....	162
Table 6.1. Thermal properties chosen to represent various units of the continental and oceanic lithosphere in the discussed model (data are from Zoth and Hänel (1988)). Start indicates a temperature-dependent parameter. A value of $1000 \text{ J Kg}^{-1} \text{ K}^{-1}$ was used for the specific heat, c , of all involved lithologies. A Nusselt number, Nu , of 4 was assumed to approximate a convective heat transfer by the hydrothermal circulation in the upper part of the oceanic crust.	246
Table 6.2. a) Sea-floor spreading rate categories (e.g., Small, 1998; Dick et al., 2003; Kriner et al., 2006).....	246
Table 6.2. b) Oceanic-continental transform slip rate categories (implied from Small, 1998; Dick et al., 2003; Kriner et al., 2006).	246

Table 6.3. Overview of all model scenarios. Hot, moderate and cold - initial equilibrium surface heat flow of 72.5, 62.5 and 52.5 mWm⁻². Nu 1 and 8 – Nusselt number of 1 and 8. v01, 03, 06 and 12 – sea-floor spreading rates of 10, 30, 60 and 120 mmy⁻¹.247

Table 6.4 Creep parameters of mafic granulite (Wilks and Carter, 1990) are assumed to represent the rheology of the lower crust in the numerical model. Within the entire range of possible lower crustal rocks, these parameters result in a moderate creep strength.256

This page intentionally left blank

Michal Nemčok, PhD

RESEARCH PROFESSOR

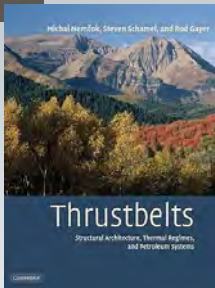
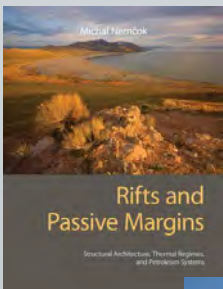


Email
mnemcok@egi.utah.edu

Phone
+421 2-2062-0781 (SK) (Office)

Research Interests

- Continental break-up processes and controlling factors
- Thrustbelt development and controlling factors
- Fracture development prediction



EMAIL:
ContactEGI@egi.utah.edu

PHONE: (801) 585-3826

Michal holds a Ph.D. in Structural Geology from the Comenius University, Bratislava. He has 35 years of applied and basic research experience at the Slovak Geological Survey, University of South Carolina, University of Wales, Cardiff, Imperial College London, University of Salzburg, University of Wurzburg, and University of Utah. He joined EGI in 1998 and is a Research Professor and Structural Group leader. Michal has published 80+ articles, coauthored 5 monographs, and coedited five books.

Continental Break-up Processes & Controlling Factors

Continental break-up research focuses on both extensional and transform settings, with a focus on driving mechanisms and controlling factors to achieve predictive models with respect to structural architecture, thermal regimes, and petroleum systems. The main research contribution includes understanding anomalous thermal and uplift histories of transform margins, break-up mechanisms in extensional settings, and micro-continent-releasing mechanisms. A summary of his last eight years of break-up research is recorded in a monograph titled *"Rifts and Passive Margins; Structural Architecture, Thermal Regimes and Petroleum Systems"* published by Cambridge University Press, and authored by Nemčok, M. Together with co-authors, a new monograph called *Strike-slip Terrains and Transform Margins—Structural Architecture, Thermal Regimes & Petroleum Systems* is being written in contract with Cambridge University Press.

Thrustbelt Development & Controlling Factors

Michal's current research focuses on the thrustbelt-foreland interactions, with a concentration on driving mechanisms and controlling factors behind thick-skin tectonics, foreland plate flexure mechanisms, and flexural faulting in control of structural architecture and play concept elements. The main research contribution includes the factors and mechanisms leading to the lack of foreland flexing and transitions from initial inversion to full accretion. Accompanying research focuses on modeling of the fluid flow mechanisms occurring in the thrustbelt front and its foreland. A summary of thrustbelt research is written in a monograph called *"Thrustbelts; Structural Architecture, Thermal Regimes and Petroleum Systems"*, published by Cambridge University Press, and authored by Nemčok, M., Schamel, S. and Gayer, R.. Current research findings are summarized in several articles included in the Geological Society of London Special Publication 377, which is edited by Nemčok, M., Mora, A., and Cosgrove, J.

Fracture Development Prediction

Fracture prediction research includes both detailed well core, rock outcrop and numerical simulation studies focused on predicting timing, location and kinematics of developing fractures. Most of the fracture studies come from thrustbelts, although some core-based studies come from various geothermal reservoirs. The main research contribution includes tools capable of predicting fracture locations, kinematics and propagation timing in two and three-dimensions for hydrocarbon reservoirs in thrustbelts, which were tested by well-based fracture data. Accompanying research includes understanding the role of mechanical stratigraphy on developing structural architecture. This research is published in a number of journals run by structural and geothermal communities.

Samuel Rybar, PhD

SEDIMENTOLOGIST



Email
srybar@egi.utah.edu

Phone
+421-915-616-570 (Slovakia)

Research Interests

- Basin analysis with focus on depositional systems and tectonics
- Well-core and outcrop sedimentology
- Petroleum system assessment with special interest in source rocks
- Paleogeography of rifted and transform margins with implications for determining sediment entry points
- 40Ar/39Ar radio-isotopic dating.

EMAIL:
ContactEGI@egi.utah.edu

PHONE: (801) 585-3826

Education & Experience

Samuel Rybar has been affiliated with EGI since 2015, working in EGI's Bratislava, Slovakia Lab, where his research focus is basin analysis with emphasis on applying standard methods of sedimentology, structural geology, tectonics, and organic geochemistry. Since 2016, Samuel has also served at the Faculty of Natural Sciences in the Department of Geology and Paleontology at Comenius University in Bratislava, Slovakia.

Samuel earned his Bachelor (2010) and Master (2012) in Geology and Paleontology and his Ph.D. in Sedimentology in 2016 from Comenius University. His Doctoral thesis title was Danube Basin Development During the Middle Miocene.

Samuel is fluent in English, Slovak, and German.

Regional & Basin Experience

- Onshore basins: Pannonian basin system, Vienna basin, Black Sea basin, Timan-Pechora basin, West Siberia basin, Volga-Ural basin, Dniiper-Donets basin.
- Offshore basins: Central and Equatorial Atlantic basins, East India basins, sheared margin basins of West Australia.

Selected Publications

Rybar, S., Šarinová K., Sant, K., Kuiper, K.F., Kováčová, M., Vojtko, R., Reiser, M.K., Fordinál, K., Teodoridis, V., Nováková, P., Vlček, T., 2019: New 40Ar/39Ar, fission track and sedimentological data on a middle Miocene tuff occurring in the Vienna Basin: implications for the North-Western Central Paratethys region. *Geologica Carpathica*, 70, 5, 386-404. doi: 10.2478/geoca-2019-0022.

Nemčok, M., **Rybar, S.**, Odegard, M., Dickson, W., Pelech, O., Ledvényiová, L., Matejová, M., Molčan, M., Hermeston, S., Jones, D., Cuervo, E., Cheng, R. & Forero, G., 2015: Development history of the southern terminus of the Central Atlantic; Guyana–Suriname case study. In: Nemčok, M., Rybar, S., Sinha, S.T., Hermeston, S.A. & Ledvényiová, L. (eds.) *Transform Margins: Development, Controls and Petroleum Systems*. Geological Society, London, Special Publications, 145-179, 431. doi: 10.1144/SP431.10

Rybar, S., Kováč, M., Šarinová, K., Halássová E., Hudáčková, N., Šujan, M., Kováčová, M., Ruman, A. & Klučiar, T. 2016: Neogene changes in paleogeography, palaeoenvironment and the provenance of sediment in the Northern Danube Basin. *Bulletin of Geosciences*, 91, 2, 367-398. doi: 10.3140/bull.geosci.1571

Nemčok, M. & **Rybar, S.**, 2016: Rift–drift transition in a magma-rich system: the Gop Rift–Laxmi Basin case study, West India. In: Mukherjee, S., Misra, A.A., Calvés, G. & Nemčok, M. (eds.) *Tectonics of the Deccan Large Igneous Province*. Geological Society, London, Special Publications, 445. doi: 10.1144/SP445.5

Júlia Kotulová, PhD

RESEARCH SCIENTIST


Email

jkotulova@egi.utah.edu

Phone

+421 905 389 667 (SK)

Research Interests

- Unconventional Gas Systems
- Organic geochemistry
- Petroleum geology
- Organic petrology
- Basin modeling (PetroMod)
- Petroleum systems
- Anoxic events
- Calibration of organic and inorganic thermometers

Júlia earned a Ph.D. in Geology, an B.Sc., RNDr. (M.Sc. equivalent) in Geology, Geochemistry and Economic geology from Comenius University, Bratislava, Slovakia. Julia joined EGI in 2011 with extensive experience as a geochemist and petroleum geologist, having spent the previous nine years working at the Department of Geophysics and Non-Renewable Energy Sources, State Geological Institute of Dionýz Štúr (Geological Survey), Bratislava, Slovak Republic. Prior to this, Julia worked with the Geological Institute at Slovak Academy of Sciences. Julia collaborates with the geochemistry lab and other researchers in the Salt Lake City office from her primary location in EGI's Bratislava office.

Research Related to Hydrocarbon Systems

- Integration of geology, geochemistry, and basin modeling for a holistic understanding of hydrocarbon generation, migration, entrapment, and preservation in order to identify regional characteristics and to de-risk new exploratory plays and prospects. Design, acquisition, implementation and interpretation of geochemical data applied to petroleum exploration and exploitation.
- Design, implementation and management rock, oil, and gas sampling and analytical programs.
- Organic geochemistry research into the molecular and isotopic composition of source rocks, oils, and gases for reservoir geochemistry, source rock quality, and thermal maturity evaluation.
- Organic petrology research with an emphasis on source rock evaluation, coal and paleoenvironmental/organic facies characterization; multi-dimensional geochemical basin modeling for the reduction of petroleum exploration risk.

Global Basin Studies

Júlia has experience with various types of basins around the globe – from the Carpathian accretionary wedge, fore-arc basins, back-arc Black Sea and Danube Basins, and the intra-arc Transcarpathian Neogene Basin to the Intermountain Basins of Slovakia – with a focus on petroleum systems, geohistorical models, thermal evolution, and fluid flow dating and duration. Her experience with passive margin basins includes the Central and Equatorial Atlantic and NW Australian margins. She also has experience with shale gas research (Central Europe, Russia, Ukraine and South America) for biogenic and thermogenic shale gas systems, geological storage of CO₂ as related to the Northern part of the Pannonian basin system, Ocean Anoxic Events research (Aptian OAE 1a and Oligocene Antarctic glaciation Oceanic Anoxic Oi-1 events), PetroMod geochemical models and Petrel 3-D geological models (East Slovakian Neogene and Intermountain Horna Nitra Neogene basins), and visual kerogen analysis (Tethys: Aptian; Paratethys: Cretaceous to Neogene in the Carpathian accretionary wedge and the Circum Black Sea region, Neogene in the North part of the Pannonian Basin).

EMAIL:

ContactEGI@egi.utah.edu

PHONE: (801) 585-3826